Electronic Supplementary Material (ESI) for Dalton Transactions.

Spin dynamics phenomena of a cerium(III) double-decker complex induced by intramolecular electron transfer

Kana Kobayashi,[a] Michiyuki Suzuki,[a] Tetsu Sato,[a] Yoji Horii,[b] Takefumi Yoshida,[c] Brian. K. Breedlove,[a] Masahiro Yamashita[a,d] and Keiichi Katoh[e]

[a.] *Department of Chemistry, Graduate School of Science, Tohoku University, 6-3, Aramaki-Aza-Aoba, Aoba-ku, Sendai, Miyagi 980-8578, Japan*

[b.] *Department of Chemistry, Faculty of Science, Nara Women's University, Kitauoya Higashimachi, Nara 630-8506, Japan*

[c.] *Cluster of Nanomaterials, Graduate School of Systems Engineering, Wakayama University, 930 Sakae-Dani, Wakayama, 640-8510, Japan.*

[d.] *School of Chemical Science and Engineering, Tongji University, Siping Road 1239, Shanghai 200092, P, R, China*

[e.] *Department of Chemistry, Graduate School of Science, Josai University, 1-1, Keyakidai, Sakaddo, Saitama 350-0295, Japan. E-mail: kkatoh@josai.ac.jp*

Table of Contents:

Table S1. Selected crystallographic data for Ce(obPc)$_2$ and TBA[Ce(obPc)$_2$] (**1**)

Complex	Ce(obPc)$_2$	TBA[Ce(obPc)$_2$] (**1**)
CCDC	2332889	2332908
Formula	$C_{128}H_{160}N_{16}O_{16}Ce$	$C_{128}H_{160}N_{16}O_{16}Ce$ $C_{16}H_{36}N$ (counter cation)
Formula weight	2495.64	2561.36
Temperature/K	153(2)	233(2)
Crystal dimension/mm	0.15 × 0.1 × 0.05	0.283 × 0.072 × 0.049
Crystal system	Monoclinic	Monoclinic
Space group	*C2/c*	*I2/a*
a/nm	46.5377(8)	33.8407(3)
b/nm	19.7134(4)	11.26360(10)
c/nm	214.1518(2)	36.7134(4)
α/deg	90	90
β/deg	114.724(2)	95.2860(10)
γ/deg	90	90
Cell volume/nm^3	11793.0(4)	13934.5(2)
Z	4	4
$F(000)$	4904.0	5460.0
ρ_{calced}/g cm^{-3}	1.306	1.221
μ/mm^{-1}	0.458	0.394
ϑ_{max}/deg	27.500	27.495
Total number of reflections	13554	15999
Number of reflections > σ threshold	11693	14721
R_1 [$I > 2\sigma(I)$]	0.0445	0.0368
wR_2 (all data)	0.1019	0.0987
Goodness of fit	1.100	1.079

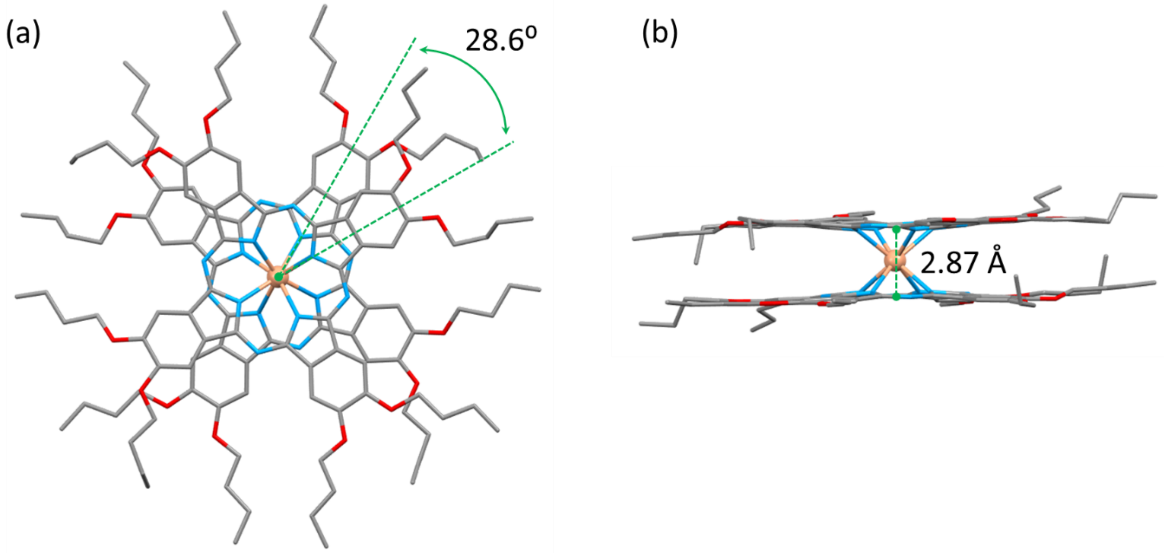

Fig. S1-1 Crystal structure of Ce(obPc)$_2$. (a) top view and (b) side view. H atom in complex omitted for clarity. Ce^{4+}: light orange, C: grey, and N: blue.

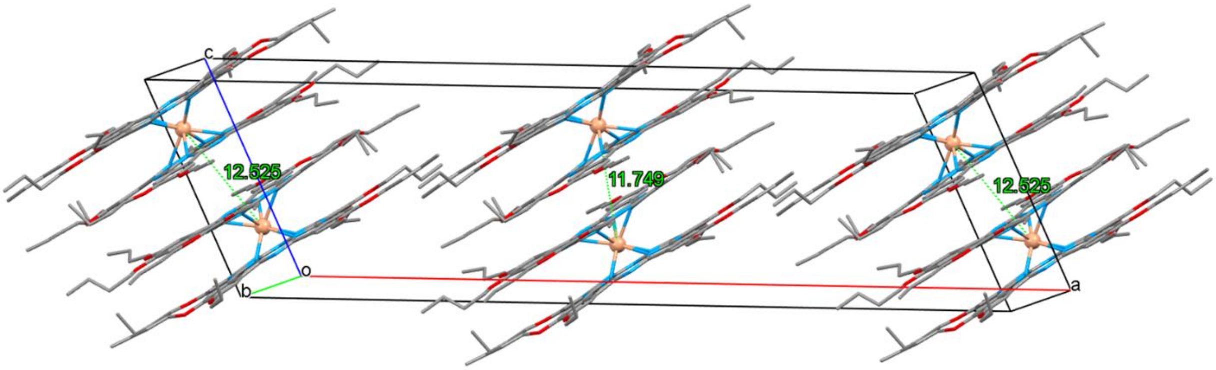

Fig. S1-2 Crystal packing of Ce(obPc)$_2$ along the *b*-axis (side view). Hydrogens were omitted for clarity. Ce^{4+}: light orange, C: grey, and N: blue.

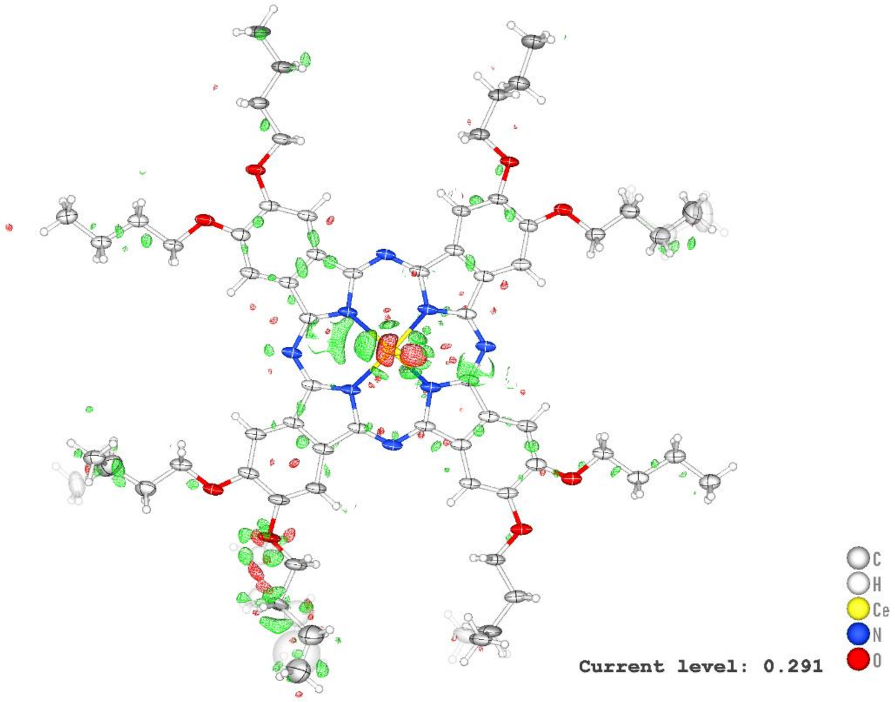

Fig. S1-3 Diagram showing the disorder processing of Ce(obPc)$_2$.

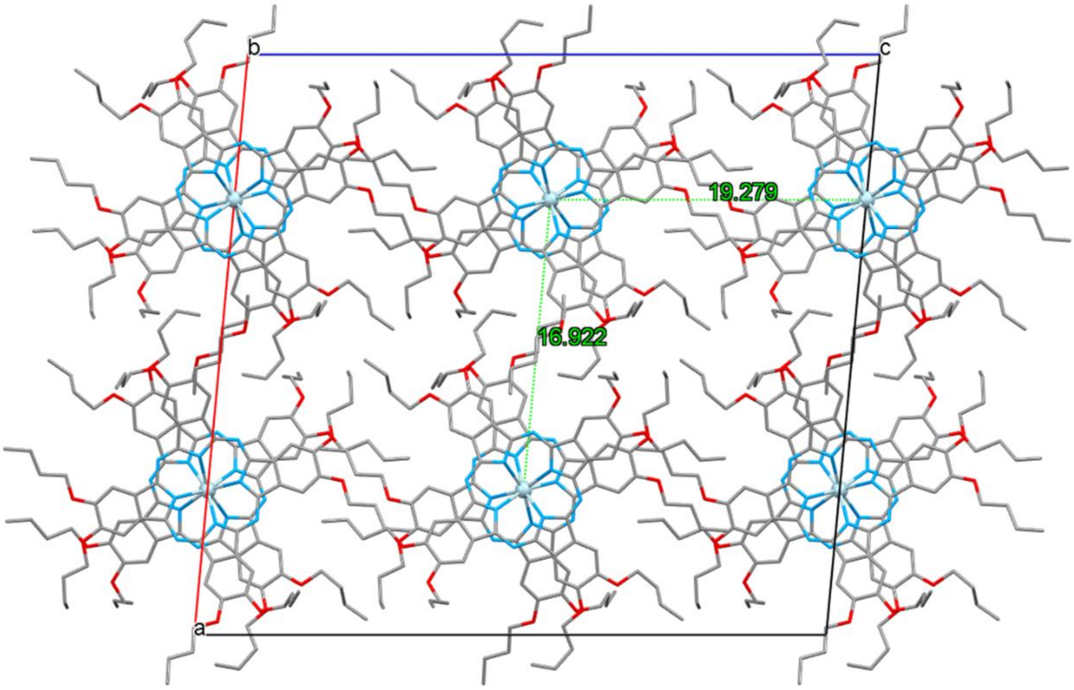

Fig. S2-1 Crystal packing of **1** in the unit cell (top view). TBA$^+$ and hydrogens were omitted for clarity. Ce^{3+}: light blue, C: grey, and N: blue.

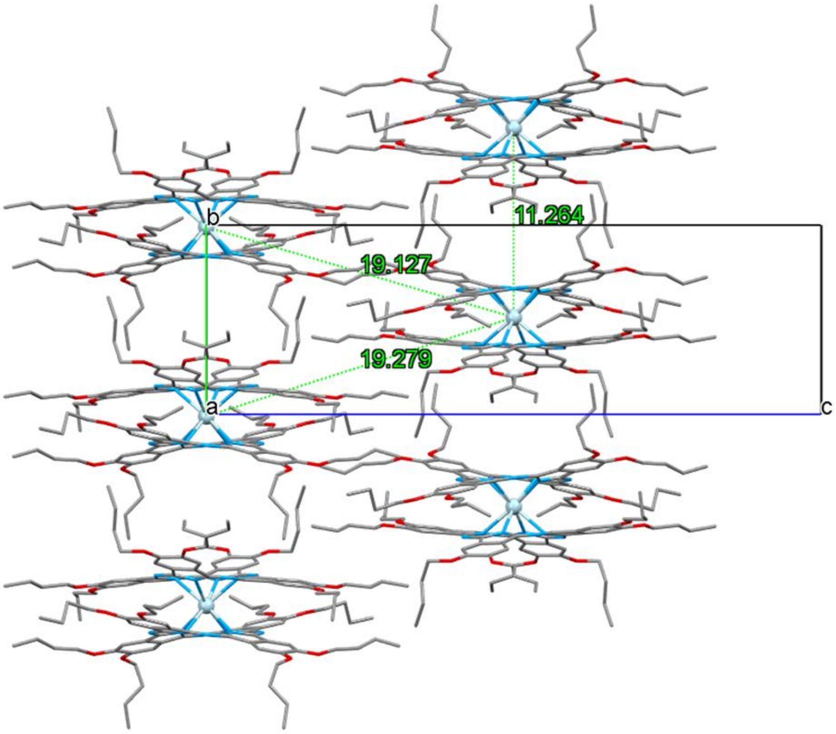

Fig. S2-2 Crystal packing of **1** along the *b*-axis (side view). TBA$^+$ and hydrogens were omitted for clarity. Ce^{3+}: light blue, C: grey, and N: blue.

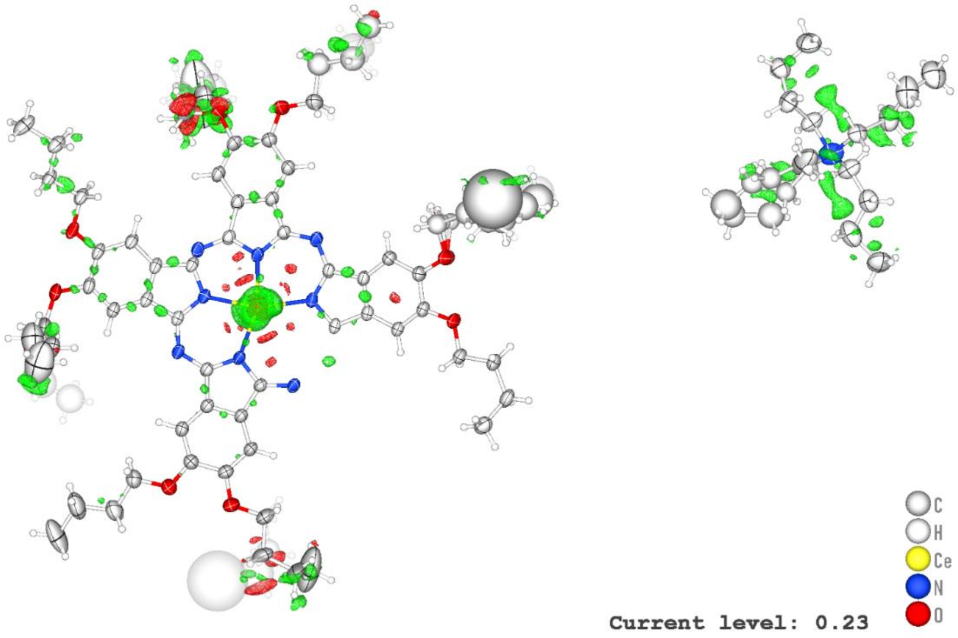

Fig. S2-3 Diagram showing the disorder processing of complex **1**.

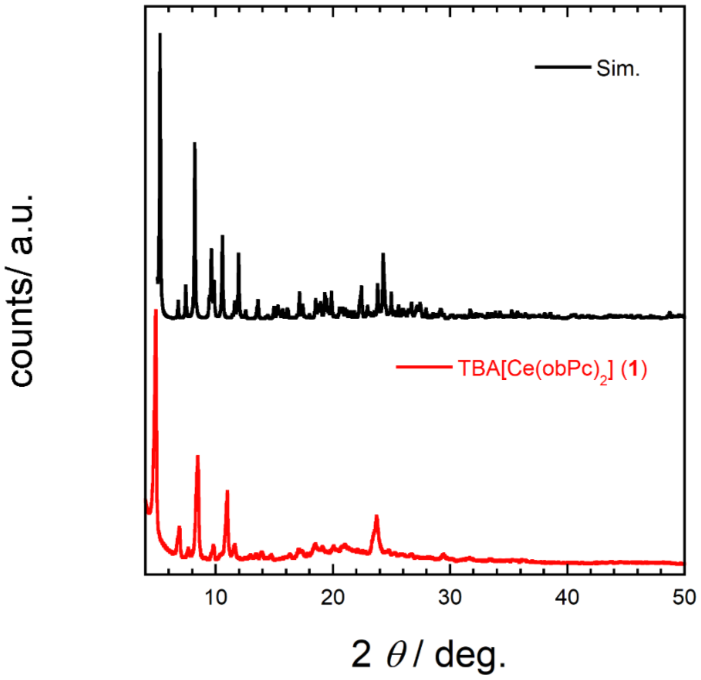

Fig. S3 PXRD pattern of **1** at 298 K. The microcrystalline PXRD and sim almost overlap, but some polymorphs are present (see main text).

Table S2. Selected crystallographic data for Ce(Pc)$_2$ and TBA[Ce(Pc)$_2$] (**2**) (This work)

Complex	Ce(Pc)$_2$	TBA[Ce(Pc)$_2$] (**2**)
CCDC	1188924[1]	148306[2]
Formula	$C_{64}H_{32}N_{16}Ce$	$C_{64}H_{32}N_{16}Ce$ $C_{16}H_{36}N$ (counter cation)
Formula weight	1165.18	1407.63
Temperature/K	100(2)	100(2)
Crystal dimension/mm	0.3 × 0.20 × 0.10	0.22 × 0.20 × 0.10
Crystal system	Monoclinic	Tetragonal
Space group	*C*2/*c*	*P*4/*ncc*
a/nm	18.7128(13)	16.8359(3)
b/nm	18.6702(9)	16.8359(3)
c/nm	15.5612(13)	22.4766(10)
α/deg	90	90
β/deg	114.369(9)	90
γ/deg	90	90
Cell volume/nm^3	4952.3(7)	6370.9(4)
Z	4	4
F(000)	2344.0	2900.0
ρ_{calced}/g cm^{-3}	1.563	1.468
μ/mm^{-1}	0.983	0.778
ϑ_{max}/deg	30.814	30.619
Total number of reflections	6948	4519
Number of reflections > σ threshold	4936	3239
R_1 [$I > 2\sigma(I)$]	0.0553	0.0539
wR_2 (all data)	0.1173	0.1278
Goodness of fit	1.030	1.071

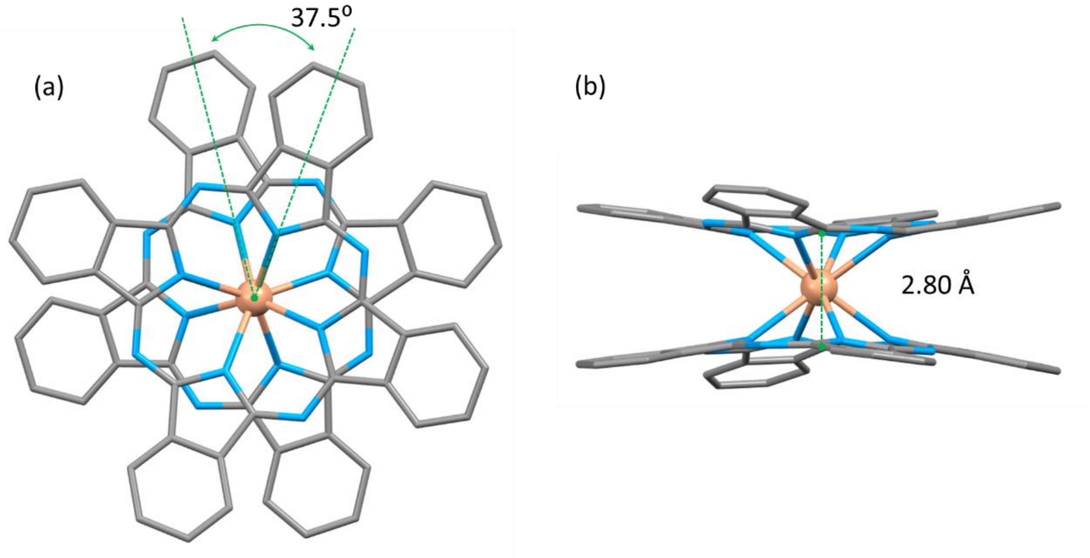

Fig. S4-1 (a) Top and (b) side views of the crystal structure of Ce(Pc)$_2$. H atom in complex omitted for clarity. Ce^{4+}: light orange, C: grey, and N: blue.

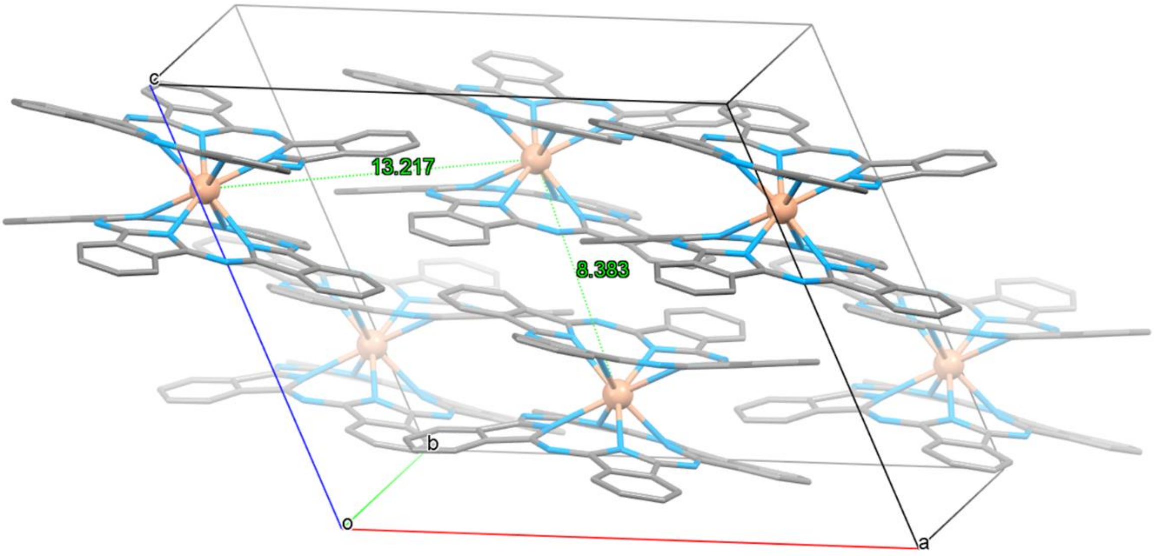

Fig. S4-2 Crystal packing of Ce(Pc)$_2$ along the *b*-axis (side view). Hydrogens were omitted for clarity. Ce^{4+}: light orange, C: grey, and N: blue.

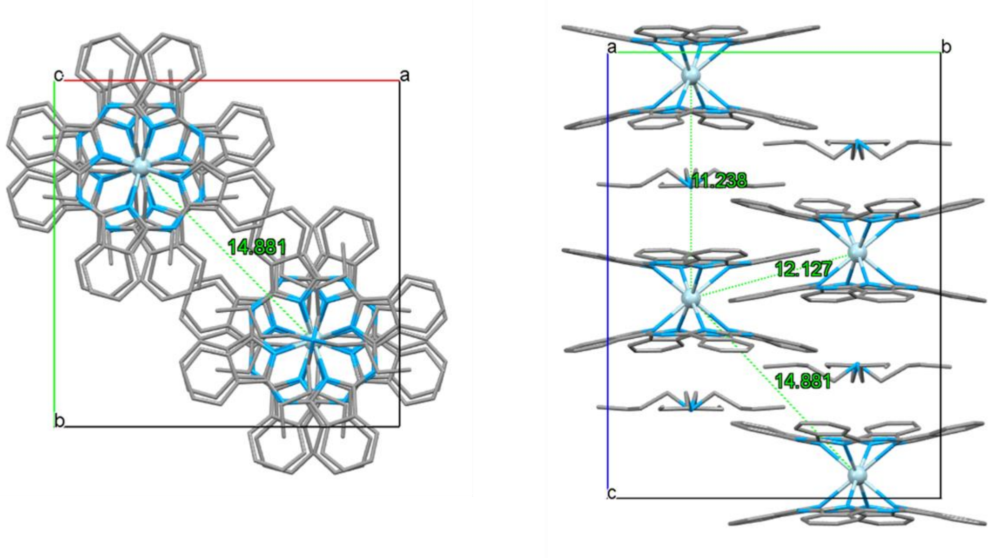

Fig. S5 Crystal packing of **2**. Hydrogen atoms were omitted for clarity. Ce^{3+}: light blue, C: grey, and N: blue.

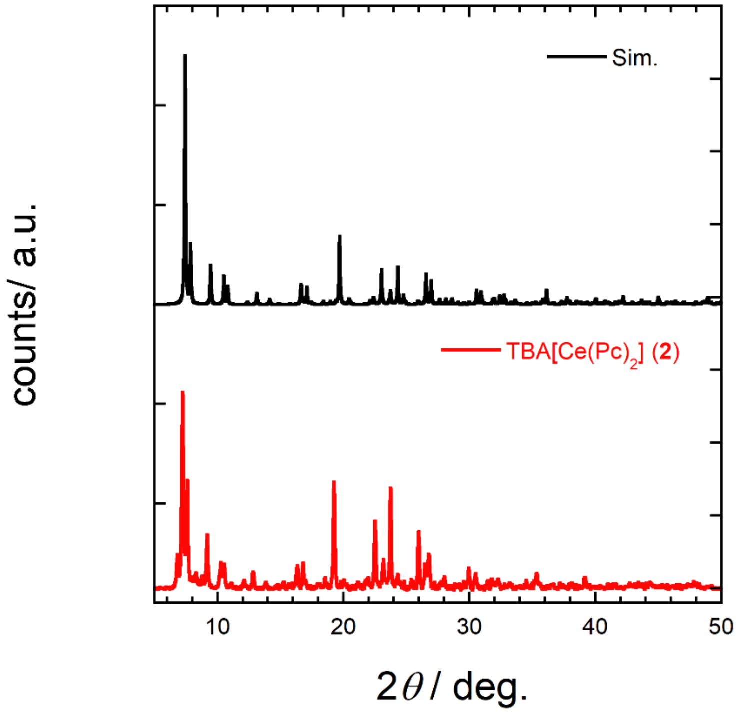

Fig. S6 PXRD pattern of **2** at 298 K. The microcrystalline PXRD pattern and the simulation almost overlap, but some polymorphs also appear (see main text).

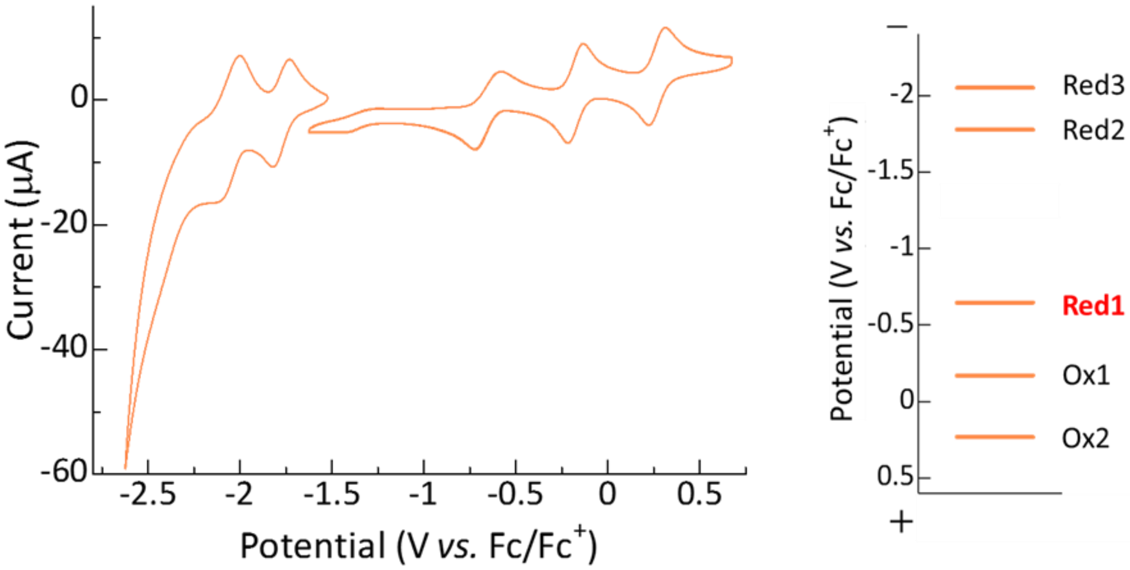

Fig. S7-1 Cyclic voltammetry (CV) of Ce(obPc)$_2$. Sample concentration 0.5 mM; glassy carbon electrode vs. Ag/Ag$^+$, 0.1 M *n*-Bu$_4$NPF$_6$ in CH$_2$Cl$_2$, v = 100 mV s^{-1}, 298 K. Potentials were referenced to a Fc/Fc$^+$ internal standard.

Table S3-1 Redox potential ($E_{1/2}$) of Ce(obPc)$_2$ in expressed in volts

Complex	$E_{1/2}^{\mathrm{Red3}}$	$E_{1/2}^{\mathrm{Red2}}$	$E_{1/2}^{\mathrm{Red1}}$	$E_{1/2}^{\mathrm{Ox1}}$	$E_{1/2}^{\mathrm{Ox2}}$
Ce(obPc)$_2$	−2.050	−1.777	−0.646	−0.170	0.232
Tb(obPc)$_2$	−2.244	−1.832	–	−0.591	−0.178

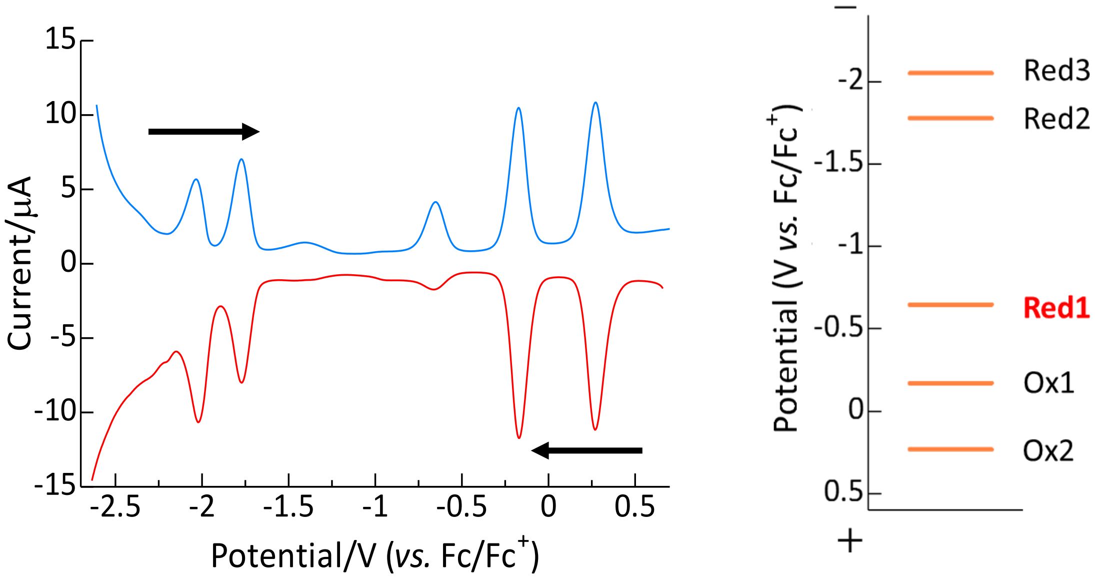

Fig. S7-2 Differential pulse voltammetry (DPV) of Ce(obPc)$_2$. Sample concentration 0.5 mM; glassy carbon working electrode vs. Ag/Ag$^+$, 0.1 M *n*-Bu$_4$NPF$_6$ in CH$_2$Cl$_2$, v = 100 mV s^{-1}, 294 K, pulse width: 50 ms, period: 0.5 s. Potentials were referenced to a Fc/Fc$^+$ internal standard.

Table S3-2. Redox potential (V) of Ce(obPc)$_2$

Complex	$E_{1/2}^{\mathrm{Red3}}$	$E_{1/2}^{\mathrm{Red2}}$	$E_{1/2}^{\mathrm{Red1}}$	$E_{1/2}^{\mathrm{Ox1}}$	$E_{1/2}^{\mathrm{Ox2}}$
Ce(obPc)$_2$	−2.033	−1.774	−0.640	−0.162	0.275
Tb(obPc)$_2$	−2.230	−1.818	–	−0.591	−0.186

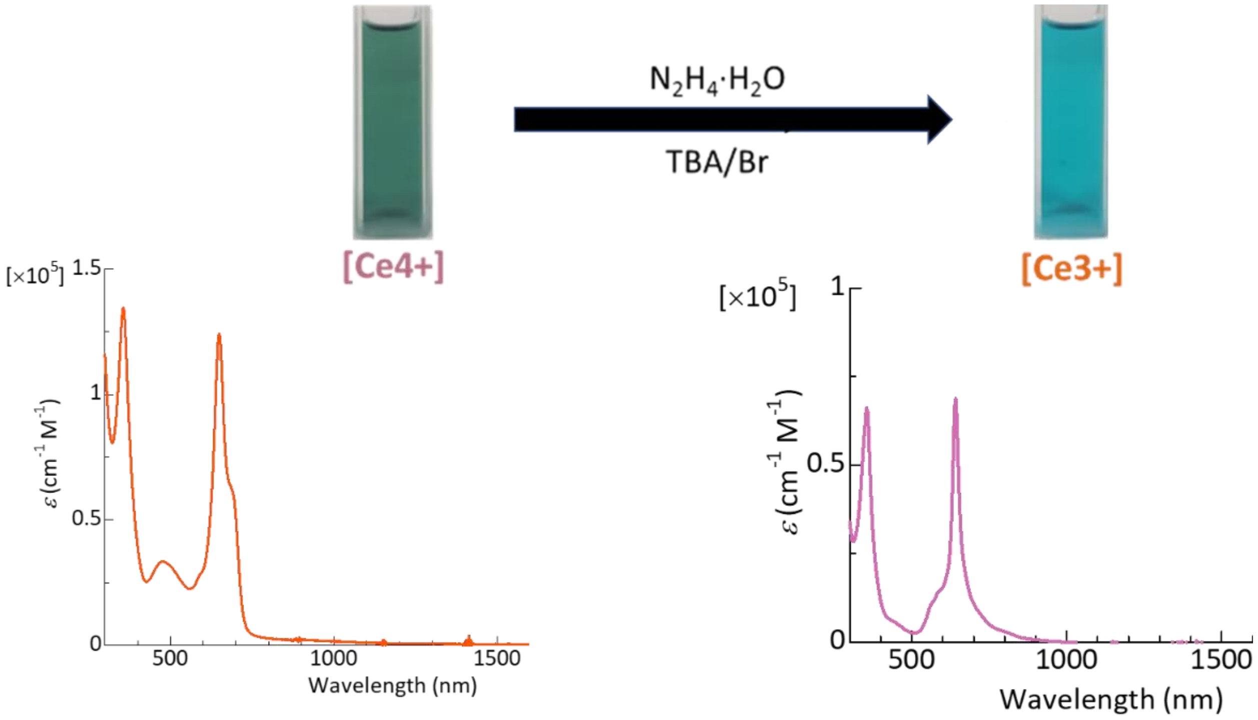

Fig. S8-1 Electronic spectra of Ce(obPc)$_2$ and TBA[Ce(obPc)$_2$] (**1**) (1.0 × 10^{-5} M) in CHCl$_3$ at 298 K.

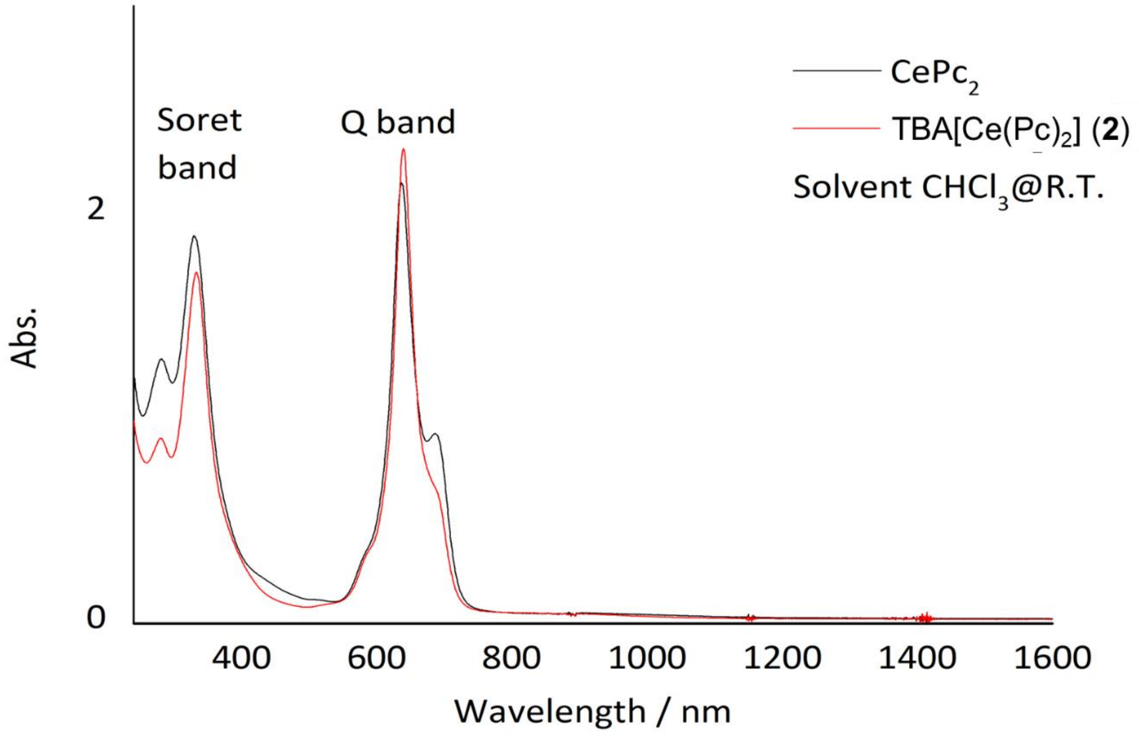

Fig. S8-2 Electronic spectra of Ce(Pc)$_2$ and TBA[Ce(Pc)$_2$] (**2**) in CHCl$_3$ at 298 K.

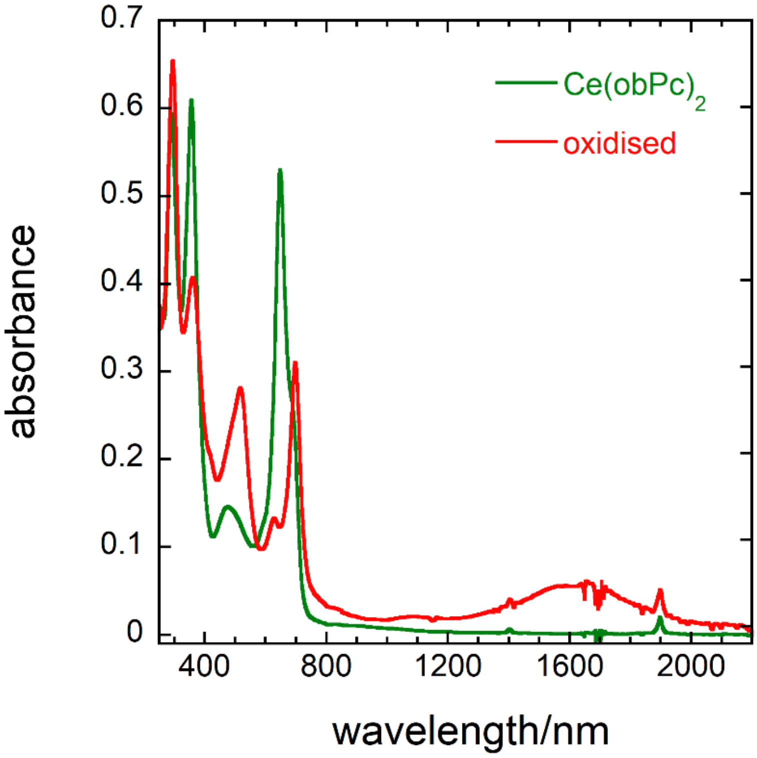

Fig. S8-3 Electronic spectra for Ce(obPc)$_2$ (10^{-6} M) in its neutral and oxidised forms in dichloromethane at 289 K. Oxidation was performed using phenoxathiine hexachloroantimonate (1.0 eq.) . The intervalence (IV) absorption band in the near-infrared region above 1200 nm suggests that there are π radicals on the Pc ligands in the $[Ce^{4+}(Pc)^{\bullet-}(Pc)^{2-}]^{+}$ unit.[3]

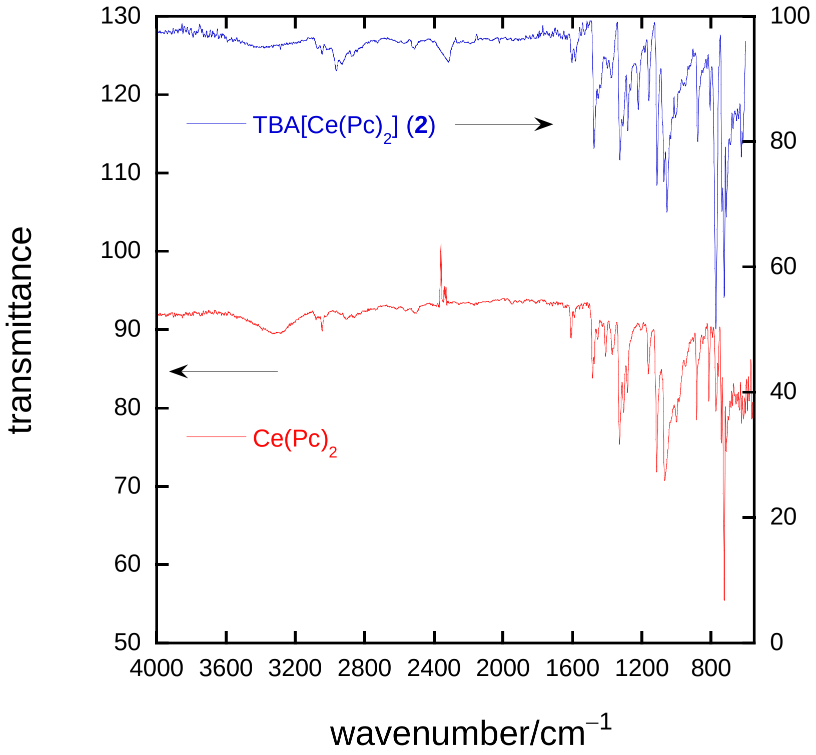

Fig. S9-1 FT-IR spectra for Ce(Pc)$_2$ and TBA[Ce(Pc)$_2$] (**2**) as KBr pellets at 298 K.

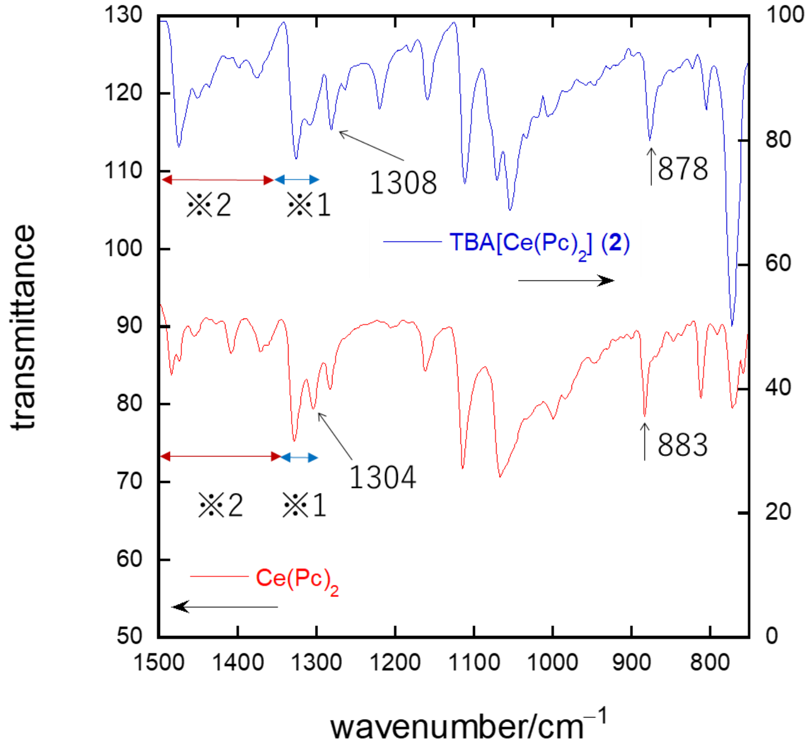

Fig. S9-2 FT-IR spectra (750–1500 cm^{-1}) for Ce(Pc)$_2$ and TBA[Ce(Pc)$_2$] (**2**) as KBr pellets at 298 K.

※1 1300–1350: pyrrole stretching. ※2 1370–1484 cm^{-1}: isoindole stretching.[4]

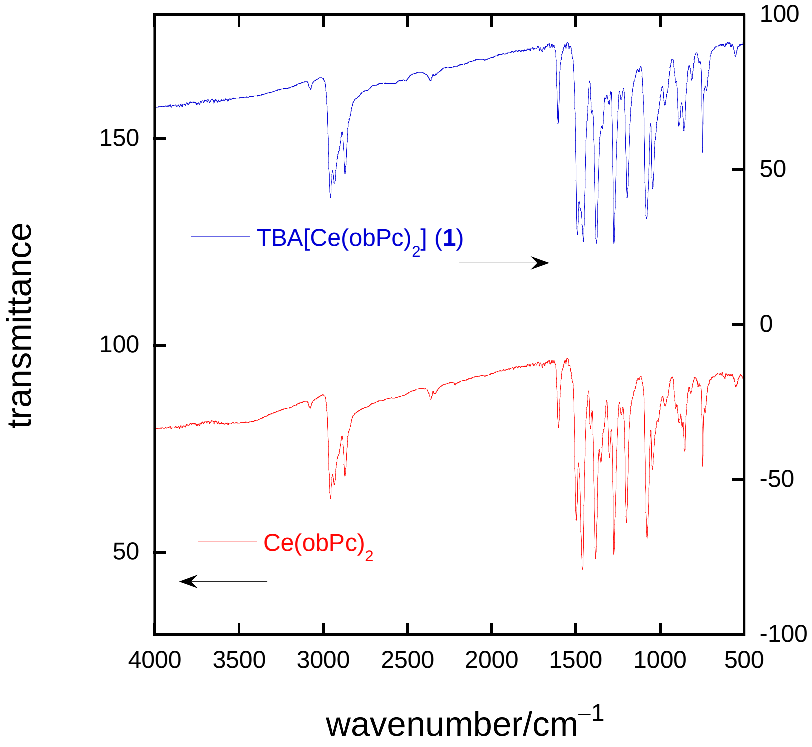

Fig. S9-3 FT-IR spectra for Ce(obPc)$_2$ and TBA[Ce(obPc)$_2$] (**1**) as KBr pellets at 289 K.

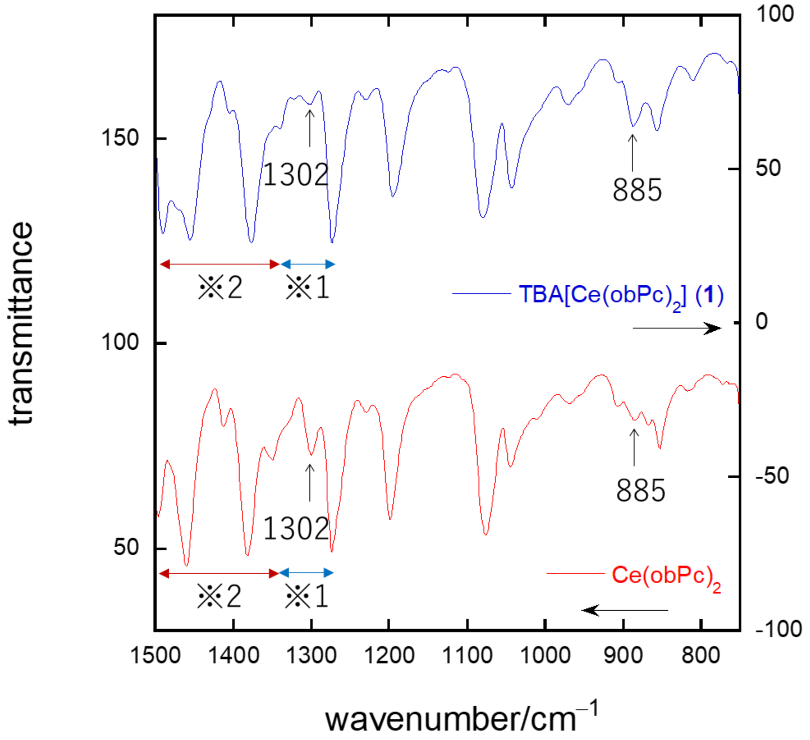

Fig. S9-4 FT-IR spectra (750–1500 cm^{-1}) for Ce(obPc)$_2$ and TBA[Ce(obPc)$_2$] (**1**) as KBr pellets at 298 K.

※1 1300–1350: pyrrole stretching. ※2 1370–1484 cm^{-1}: isoindole stretching.[4]

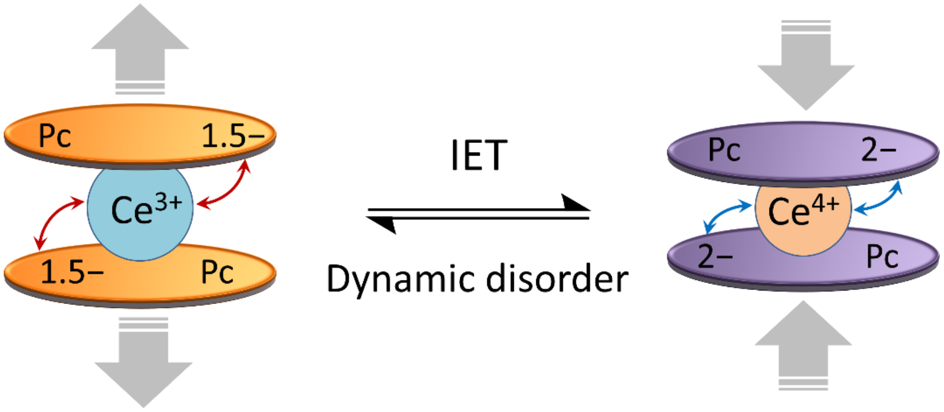

Fig. S10 Schematic illustration of the intramolecular electron transfer (IET) for neutral Ce(obPc)$_2$ and Ce(Pc)$_2$ with the dynamic disorder (see main text).

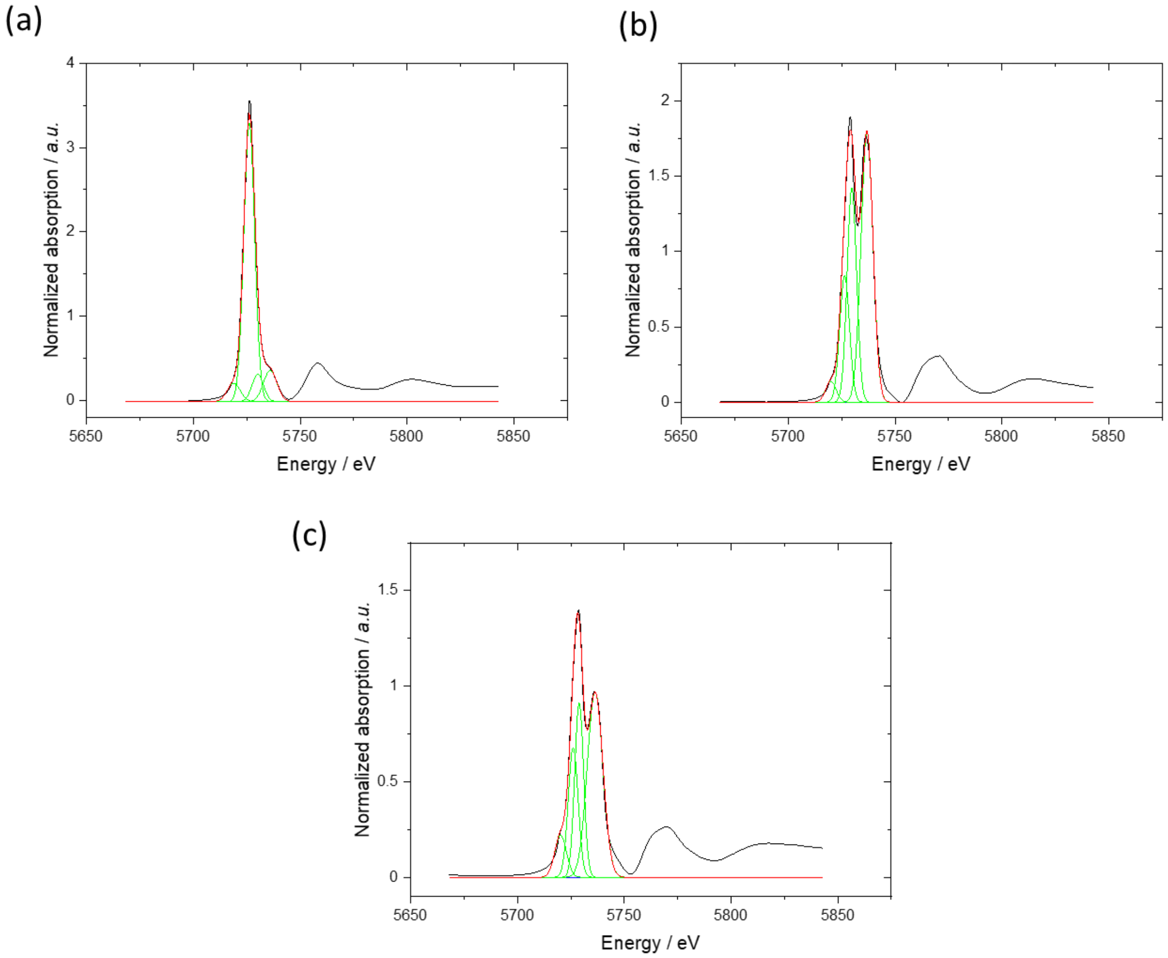

Fig. 11 Ce L$_{III}$-edge XANES spectra of Ce(Pc)$_2$ based complexes. (a) TBA[Ce(obPc)$_2$] (**1**), (b) Ce(obPc)$_2$, and (c) Ce(Pc)$_2$. Deconvolution analysis was performed based on the literature.[5,6] The solid lines show the results of estimating the components of Ce^{3+} and Ce^{4+} using a Gaussian function.

Table S4-1. Deconvolution analysis data of area ratio for the Ce(Pc)$_2$ based complexes in Fig. S11

Peak	Position (*E*/eV)	Ce(obPc)$_2$	Ce(Pc)$_2$	**1**
Pre-edge	5721	0.18	0.38	0.76
a	5726	1.0	1.0	9.6
b	5729	1.65	1.2	1.0
c	5736	2.63	2.26	1.3

Table S4-2. Deconvolution analysis data for the Ce(Pc)$_2$-based complexes in Fig. S11

Ce complex	**method**	**Area ratio Ce^{3+}:Ce^{4+}**	**Percentage(%) Ce^{3+}:Ce^{4+}**	**Net valence of Ce ion**	**Method Ref.**
TBA[Ce(obPc)$_2$]	(A)	10.4:2.3	82:18	3.2	5
(**1**)	(B)	10.6:1.3	89:11	3.1	6
Ce(obPc)$_2$	(A)	1.2:4.3	22:78	3.8	5
	(B)	2.7:5.3	51:49	3.5	6
Ce(Pc)$_2$	(A)	1.4:3.9	26:74	3.7	5
	(B)	2.6:4.9	53:47	3.5	6

§ Methods for estimating the valence of Ce ion vary depending on the researcher. We used two methods to estimate the Ce valence of the Ce(Pc)$_2$-based complexes. (A) The ratio was calculated assuming that Pre-edge and **a** are derived from Ce^{3+} (4f^1), and **b** and **c** are derived from Ce^{4+} (4f^0).[5] (B) The ratio was calculated assuming that **a** and **b** were derived from Ce^{3+} (4f^1) and **c** was derived from Ce^{4+} (4f^0).[6]

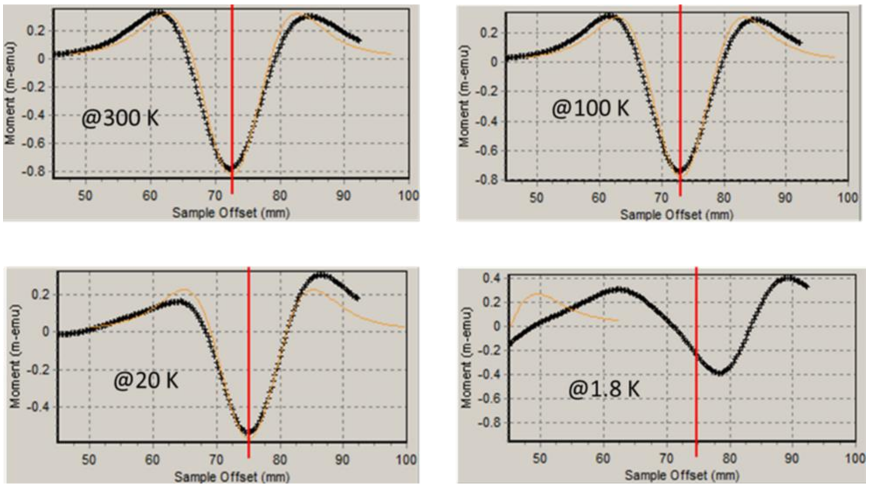

Fig. S12 In the magnetic measurements, while conducting the centering process to ascertain the precise position of the sample, response curves are procured. If the response curve manifests upward convexity, it signifies the paramagnetic nature of the sample. In contrast, the presence of downward convexity, even in strong magnetic field intensities and high temperatures nearing 2 K, denotes the diamagnetic character of the sample. Measurements of Ce(obPc)$_2$ were executed at 300 K, 100 K, 20 K, and 1.8 K in a 10 kOe dc magnetic field. In Ce(obPc)$_2$, diamagnetic response curves were generated across all temperature regimes. Samples that were prepared using a Ce^{3+} precursor showed no traces of Ce^{3+} in the sample (see Experimental section in main text).

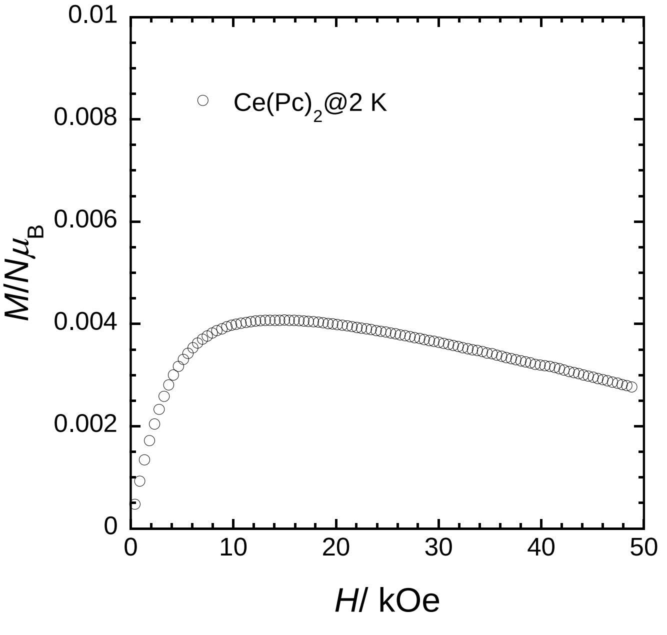

Fig. S13 *M-H* curve for powder samples of Ce(Pc)$_2$. It exhibits paramagnetic properties at 2 K. On the other hand, it exhibited diamagnetic properties above 10 K. Samples that were prepared using a Ce^{4+} precursor showed traces of Ce^{3+} in the sample (see Experimental section in main text). Thus, both Ce(obPc)$_2$ and Ce(Pc)$_2$ are in a Ce^{4+}/Ce^{3+} mixed valence state, with the paramagnetic signature observed for Ce(Pc)$_2$ indicative of a higher ratio of Ce^{3+} in comparison to Ce(obPc)$_2$ (Table S4).

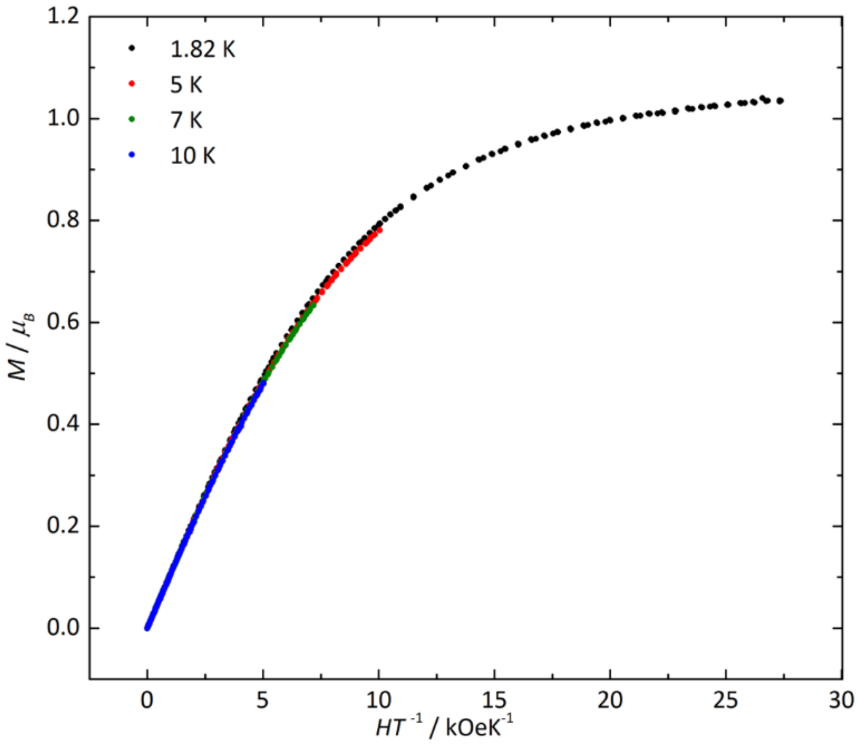

Fig. S14 Reduced magnetization (M versus HT^{-1}) for powder samples of **2**.

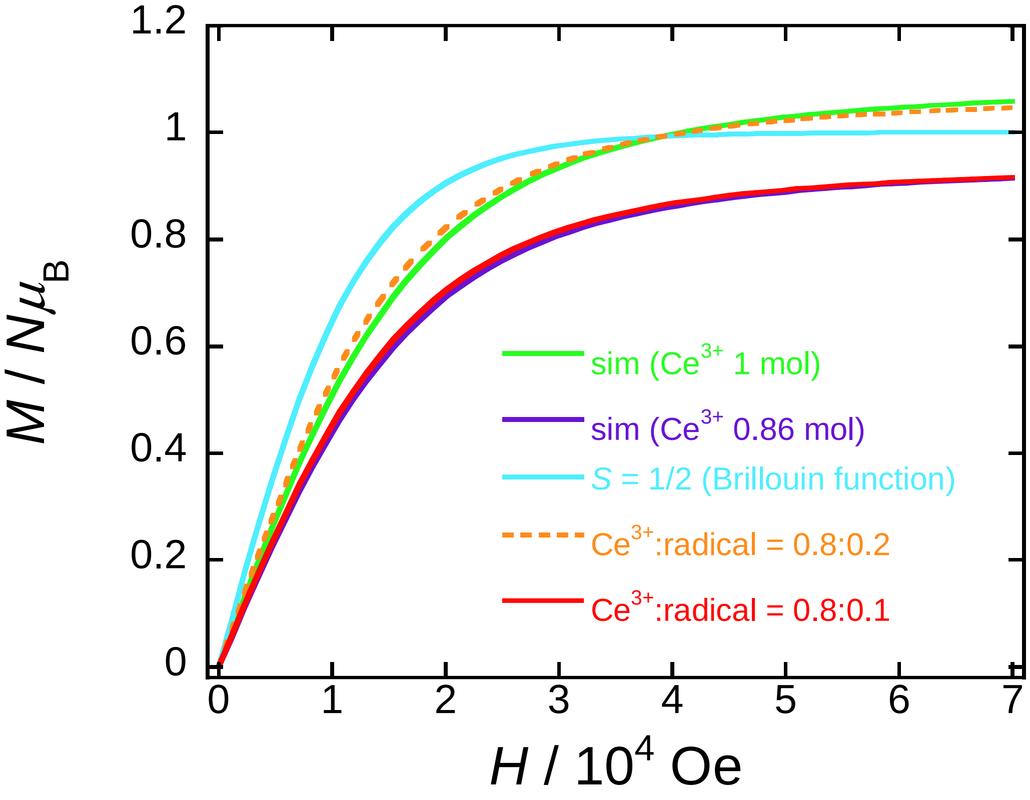

Fig. S15 As a supplement to Fig. 5, simulation results of the *M*-*H* curve are presented. The simulation curve indicates that the yellow-green line represents 1 mol of Ce^{3+} using LFPs. The cyan line represents a radicals delocalized on Pc ligands using Brillouin function with S = 1/2 (1 mol). The purple line, using LFPs with 0.86 mol of Ce^{3+}, reproduced the experimental data (see Fig. 5). This is effective when assuming Ce^{3+}:Ce^{4+} = 0.8:0.2 based on XANES spectrum analysis (Table S4-2) and attributing magnetic properties to the Ce^{3+} component.

On the other hand, the orange dashed line represents the result of simulation at [Ce^{3+}(obPc)$^{2-}$(obPc)$^{2-}$]$^-$:[Ce^{4+}(obPc)$^{2-}$(obPc)$^{\bullet 3-}$]$^-$ = Ce^{3+}:radical = 0.8:0.2 based on XANES spectrum analysis, which fails to reproduce the experimental data (see Fig. 5). The experimental values can be nearly reproduced by the red line (Ce^{3+}:radical = 0.8:0.1). These simulations simply add together Ce^{3+} and radical components. Considering the XANES spectrum of the neutral species (Table S4-2) and the results of *M*-*H* (Fig. S13), the magnetisation value of the radicals in the [Ce^{4+}(obPc)$^{2-}$(obPc)$^{\bullet 3-}$]$^-$ unit resulting from intramolecular electron transfer (IET) are lower than the ratio obtained from XANES spectrum.

Table S5-1. Wavefunction composition (in %) of the $^{2}F_{5/2}$ states of $[Ce(Pc)_2]^-$

M_J	w.f. 1	w.f. 2	w.f. 3	w.f. 4	w.f. 5	w.f. 6
-5/2	98.5	0.0	0.0	1.5	0.0	0.0
-3/2	0.0	1.5	98.3	0.2	0.0	0.0
-1/2	0.0	0.0	0.0	0.0	86.5	13.5
+1/2	0.0	0.0	0.0	0.0	13.5	86.5
+3/2	1.5	0.0	0.2	98.3	0.0	0.0
+5/2	0.0	98.5	1.5	0.0	0.0	0.0

Table S5-2. Wavefunction composition (in %) of the $^{2}F_{5/2}$ states of $[Ce(obPc)_2]^-$

M_J	w.f. 1	w.f. 2	w.f. 3	w.f. 4	w.f. 5	w.f. 6
-5/2	96.0	3.2	0.6	0.0	0.0	0.2
-3/2	0.0	0.7	0.1	46.0	49.7	3.5
-1/2	0.1	0.0	53.2	0.1	3.1	43.5
+1/2	0.0	0.1	0.1	53.2	43.5	3.1
+3/2	0.7	0.0	46.0	0.1	3.5	49.7
+5/2	3.2	96.0	0.0	0.6	0.2	0.0

Table S5-3. Calculated *g*-tensor for the Kramers doublets (KD)

	$[Ce(Pc)_2]^-$			$[Ce(obPc)_2]^-$		
	g_x	g_y	g_z	g_x	g_y	g_z
KD1	0.61	0.61	3.96	0.40	0.51	4.01
KD2	0.89	0.89	1.50	0.42	1.31	3.18
KD3	2.52	2.52	0.80	0.63	1.30	3.16

Table S6. Ligand field parameters obtained from ab initio calculations

k	*q*	*B*(*k*,*q*) / cm^{-1}	*B*(*k*,*q*) / cm^{-1}
		[Ce(Pc)$_2$]$^-$	[Ce(obPc)$_2$]$^-$
2	-2	-0.0015308	14.097661
2	-1	-0.0084485	0.01661913
2	0	972.89188	1030.46862
2	1	0.003407	0.00347098
2	2	-0.0219653	-142.56892
4	-4	0.0004892	0.00217146
4	-3	-0.0013144	7.70871517
4	-2	-0.0031819	0.00198782
4	-1	-97.991263	14.937797
4	0	-148.20931	-185.40017
4	1	-6.587E-05	-0.0019471
4	2	0.0026363	-12.254691
4	3	0.0004801	-0.0015113
4	4	124.06587	-117.20673

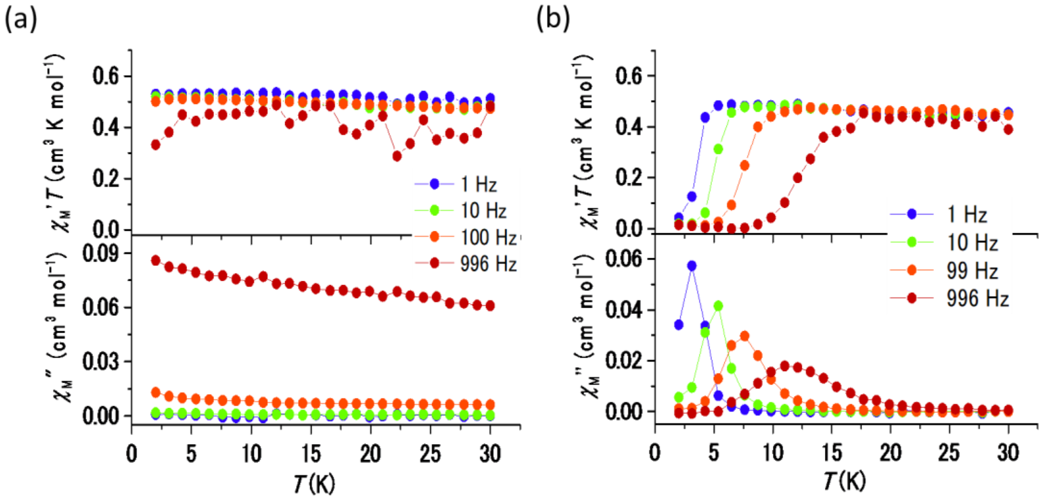

Fig. S16-1 (a) Frequency (*ν*) dependences of the (top) in-phase (χ_M') and (bottom) out-of-phase (χ_M'') ac magnetic susceptibilities of **1** in an H_{dc} of zero Oe. (b) *ν* dependences of the (top) in-phase (χ_M') and (bottom) out-of-phase (χ_M'') ac magnetic susceptibilities of **1** in an H_{dc} of 250 Oe. The solid lines are guides only.

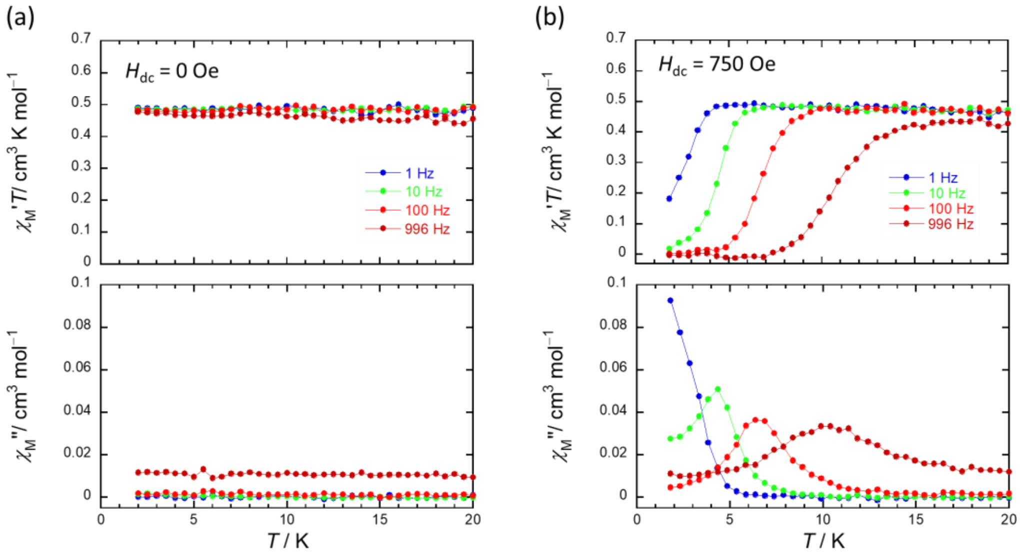

Fig. S16-2 (a) Frequency (*ν*) dependences of the (top) in-phase (χ_M') and (bottom) out-of-phase (χ_M'') ac magnetic susceptibilities of **2** in an H_{dc} of zero Oe. (b) *ν* dependences of the (top) in-phase (χ_M') and (bottom) out-of-phase (χ_M'') ac magnetic susceptibilities of **2** in an H_{dc} of 750 Oe. The solid lines are guides only.

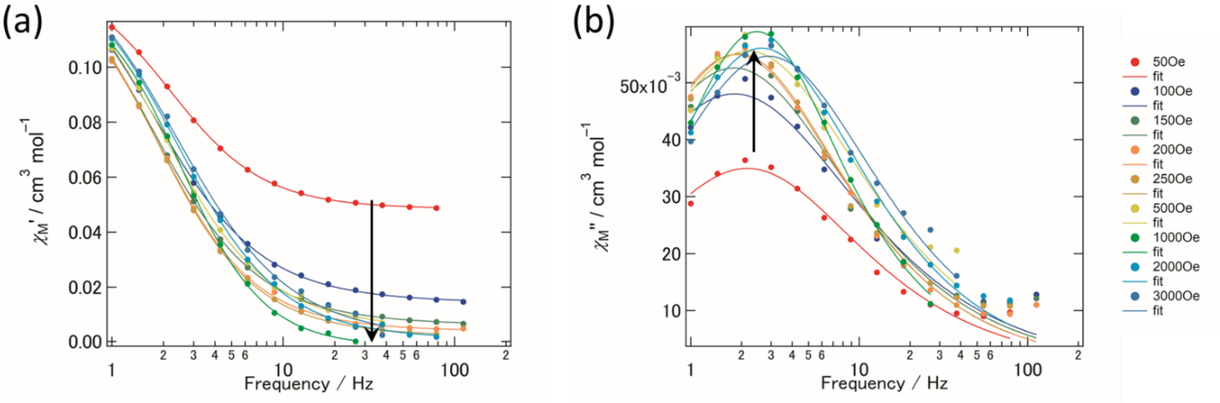

Fig. S17 Frequency (ν) dependences of the (a) in-phase (χ_M') and (b) out-of-phase (χ_M'') ac magnetic susceptibilities of **1** at 4 K in several dc magnetic fields. The solid lines were fitted by using eqns. S1−S3.

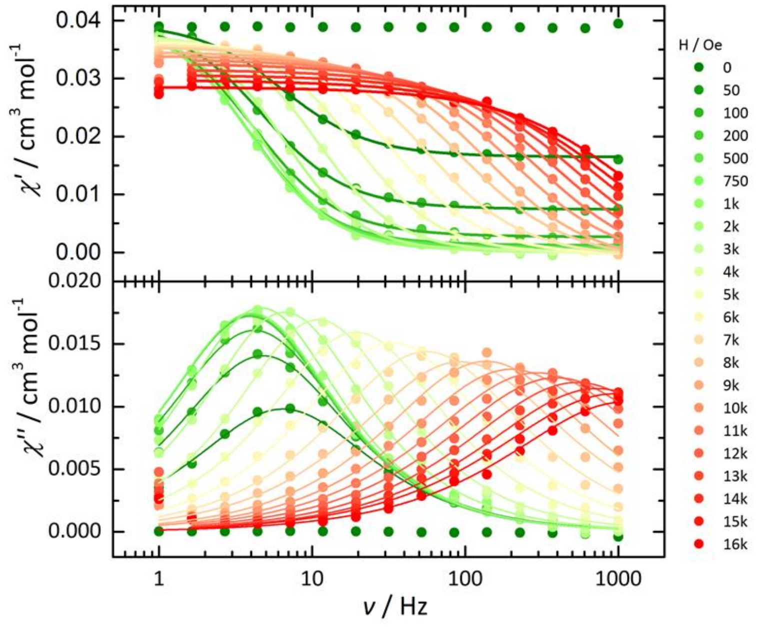

Fig. S18 Frequency (ν) dependences of the (a) in-phase (χ_M') and (b) out-of-phase (χ_M'') ac magnetic susceptibilities of **2** at 4 K in several dc magnetic fields. The solid lines were fitted by using eqns. S1−S3.

Generalized Debye model (eqns. S1–S3)[7]

The real ($\chi_M{}'$) and imaginary parts ($\chi_M{}''$) of the ac magnetic susceptibilities are determined by using eqns. S2 and S3, respectively.

$$\chi_{total}(\omega) = \chi_S + \frac{\chi_T - \chi_S}{1 + (i\omega\tau)^{1-\alpha}} \qquad \text{(eqn. S1)}$$

$$\chi'(\omega) = \chi_S + (\chi_T - \chi_S)\frac{1 + (\omega\tau)^{1-\alpha}\sin(\pi\alpha/2)}{1 + 2(\omega\tau)^{1-\alpha}\sin(\pi\alpha/2) + (\omega\tau)^{2-2\alpha}} \qquad \text{(eqn. S2)}$$

$$\chi''(\omega) = (\chi_T - \chi_S)\frac{(\omega\tau)^{1-\alpha}\cos(\pi\alpha/2)}{1 + 2(\omega\tau)^{1-\alpha}\sin(\pi\alpha/2) + (\omega\tau)^{2-2\alpha}} \qquad \text{(eqn. S3)}$$

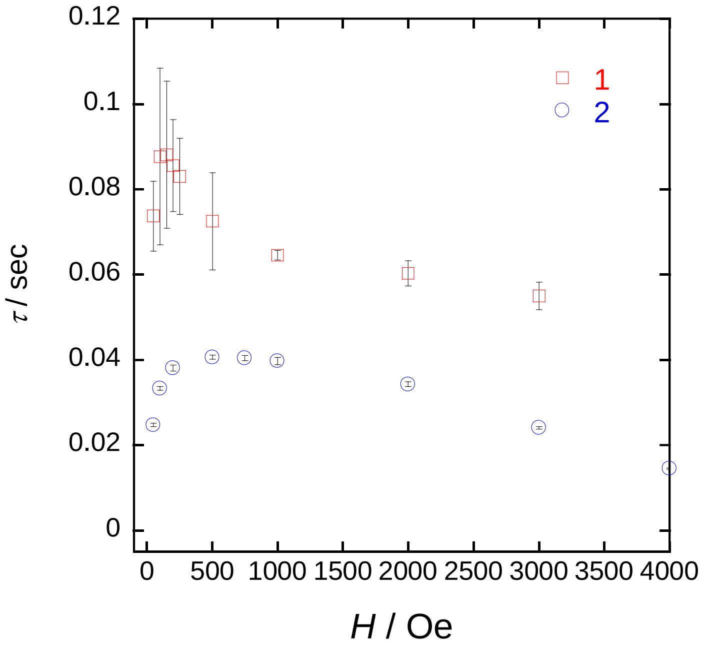

Fig. S19 H_{dc} dependence (zero–4000 Oe) of τ for **1** and **2** at 4 K.

Table S7. Optimised parameters of **2** in Fig. 6a

complex	a_1	a_2	b	c
2	55.187	0.0010259	4.523e-14	24.99

§ Optimized parameters for **1** are not listed because there is no data up to high magnetic fields and large error bars.

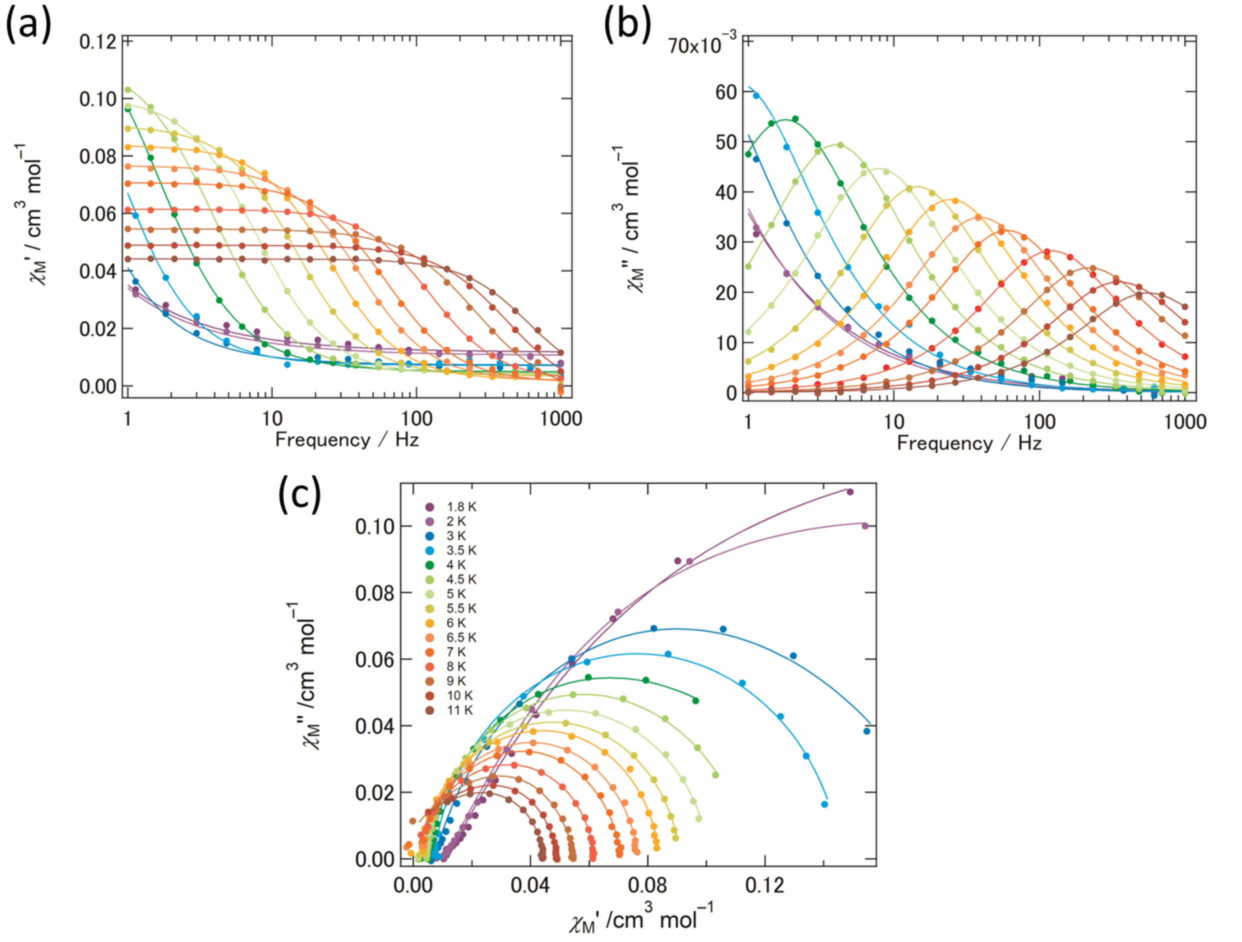

Fig. S20 Frequency (*ν*) and temperature (*T*) dependences of the (a) in-phase ($\chi_M{}'$) and (b) out-of-phase ($\chi_M{}''$) ac magnetic susceptibilities of **1** in an H_{dc} of 250 Oe. The solid lines were fitted by using eqns. S1–S3. The semicircular Argand plots with the small *α* parameters (0.02–0.28) confirm that slow magnetic relaxation occurs via a single process.

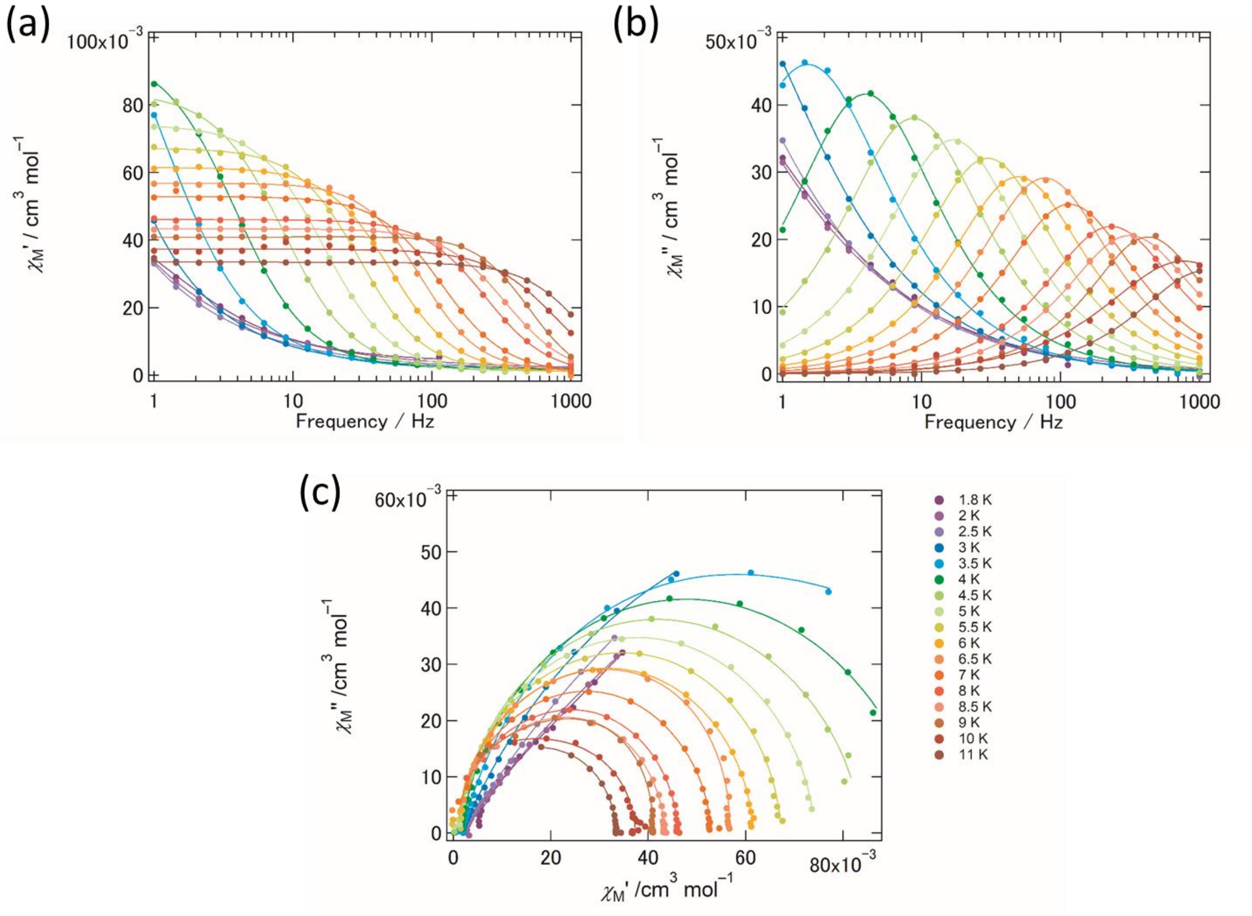

Fig. S21 Frequency (ν) and temperature (T) dependences of the (a) in-phase (χ_M') and (b) out-of-phase (χ_M'') ac magnetic susceptibilities of **2** in an H_{dc} of 750 Oe. The solid lines were fitted by using eqns. S1−S3. The semicircular Argand plots with the small α parameters (0.002−0.28) confirm that slow magnetic relaxation occurs via a single process (> 3 K).

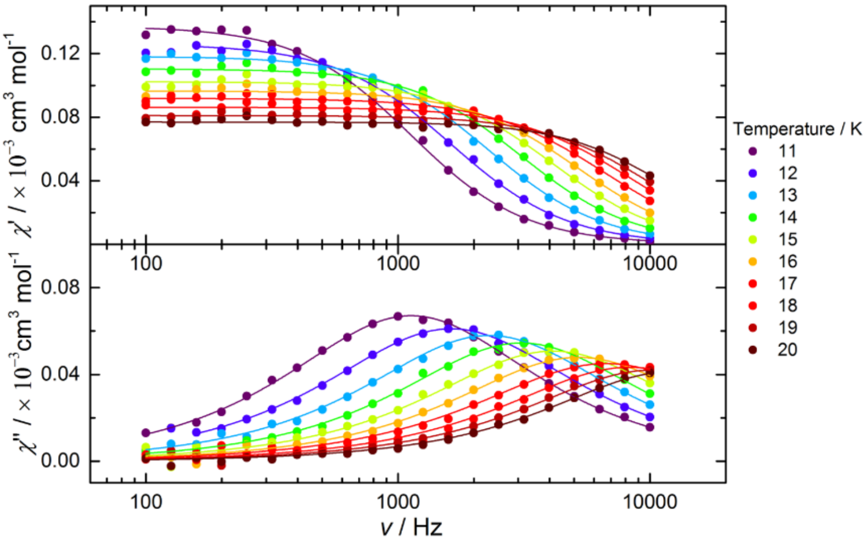

Fig. S22 Frequency (ν) and temperature (T = 11–20 K) dependences of the (a) in-phase (χ_M') and (b) out-of-phase (χ_M'') ac magnetic susceptibilities of **2** in an H_{dc} of 750 Oe. The solid lines were fitted by using eqns. S1–S3.

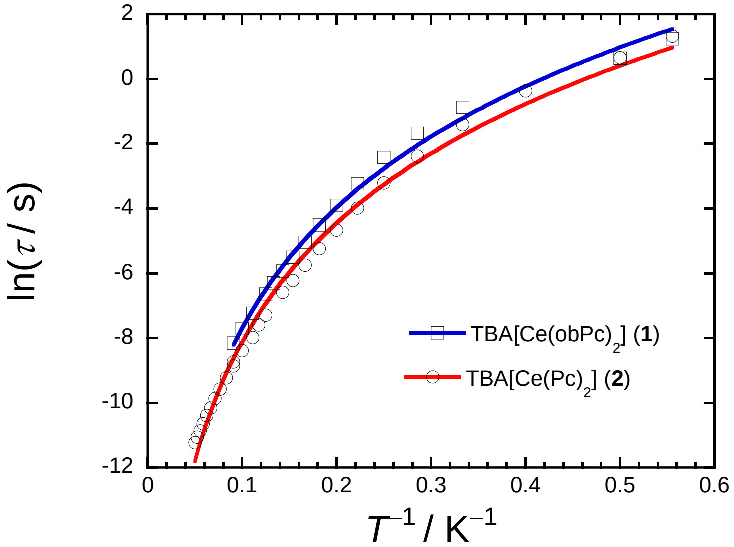

Fig. S23 An Arrhenius plot of **1** (open square) and **2** (open circles), for which the τ values were obtained from χ_M'' versus ν plots. The solid lines were fitted by using $\tau^{-1} = CT^m$, respectively. See main text.

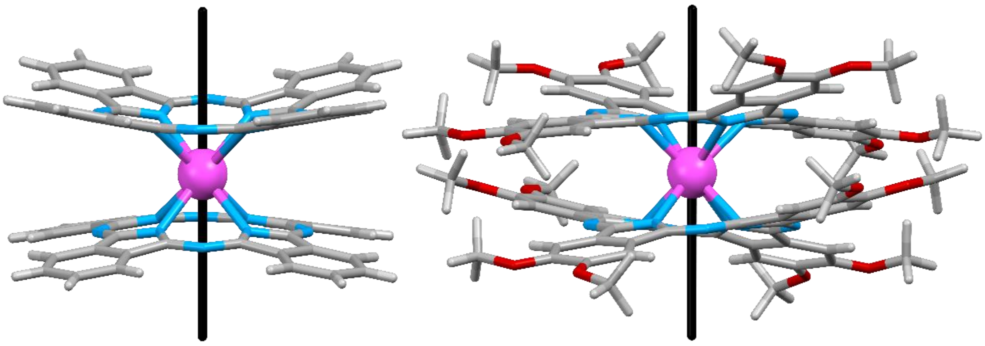

Fig. S24 Magnetic axis of the ground doublet of $[Ce(Pc)_2]^-$ (left) and $[Ce(obPc)_2]^-$ (right).

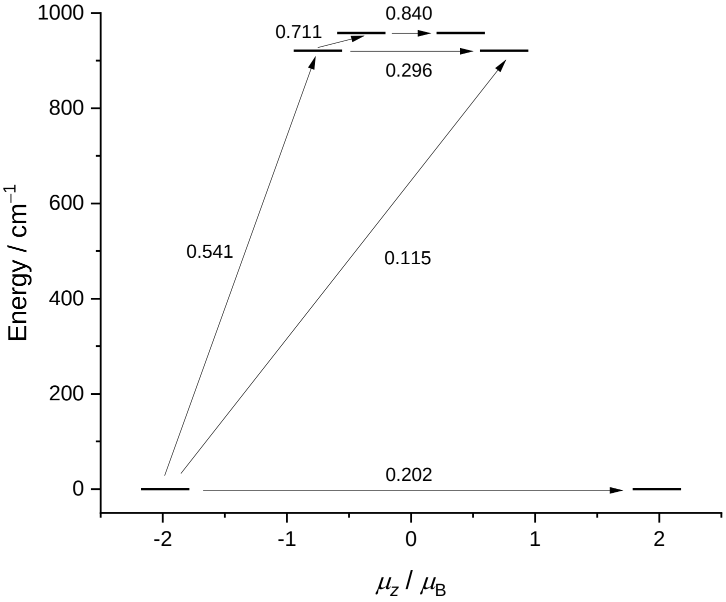

Fig. S25-1 Ligand field splitting of $[Ce(Pc)_2]^-$. The arrows indicate the relaxation pathway with the transition magnetic moment in units of μ_B.

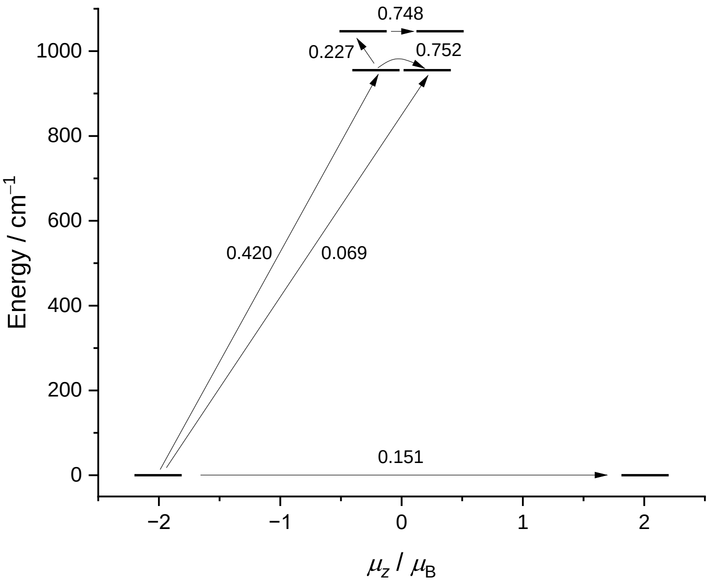

Fig. S25-2 Ligand field splitting of [Ce(obPc)$_2$]$^-$. The arrows indicate the relaxation pathway with the transition magnetic moment in units of μ_B.

Table S7. Energy levels of $^2F_{5/2}$ states

	Energy / cm^{-1}	Energy / cm^{-1}
	[Ce(Pc)$_2$]$^-$	[Ce(obPc)$_2$]$^-$
w.f. 1	0	0
w.f. 2	0	0
w.f. 3	921	955
w.f. 4	921	955
w.f. 5	958	1047
w.f. 6	958	1047

References

1 M. S. Haghighi, C. R. L. Teske and H. Honborg, *Zeitschrift für Anorg. und Allg. Chemie*, 1992, **608**, 73–80.

2 H. Hückstädt, A. Tutaß, M. Göldner, U. Cornelissen and H. Homborg, *Z. Anorg. Allg. Chem*, 2001, **627**, 485–497.

3 T. H. Tran-Thi, T. A. Mattioli, D. Chabach, A. D. Cian and R. Weiss, *J. Phys. Chem.*, 1994, **98**, 8279–8288.

4 F. Lu, M. Bao, C. Ma, X. Zhang, D. P. Arnold and J. Jiang, *Spectrochim. Acta - Part A Mol. Biomol. Spectrosc.*, 2003, **59**, 3273–3286.

5 J. El Fallah, S. Boujana, H. Dexpert, A. Kiennemann, J. Majerus, O. Touret, F. Villain and F. Le Normand, *J. Phys. Chem.*, 1994, **98**, 5522–5533.

6 A. Bianconi, A. Marcelli, H. Dexpert, R. Karnatak, A. Kotani, T. Jo and J. Petiau, *Phys. Rev. B*, 1987, **35**, 806–812.

7 K. S. Cole and R. H. Cole, *J. Chem. Phys.*, 1941, **I**, 341–351.